Organic Electronics 113 (2023) 106712

Contents lists available at ScienceDirect

Organic Electronics

journal homepage: www.elsevier.com/locate/orgel

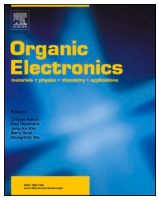

Energy level alignment studies in tin perovskite solar cells through incorporation of inorganic cation and charge transport layer selection

Muhammad Akmal Kamarudin [a,**,1], Shahrir Razey Sahamir [a,*,1], Teresa S. Ripolles [b], Kohei Nishimura [a], Shen Qing [c], Shuzi Hayase [a,***]

[a] i-Powered Energy System Research Center (i-PERC), The University of Electro-Communications, 1-5-1 Chofugaoka, Chofu, Tokyo, 182-8585, Japan
[b] Spain Instituto de Ciencia de los Materiales, University of Valencia, C/Catedrátic José Beltrán Martinez, 2, Paterna, 46980, Valencia, Spain
[c] Faculty of Informatics and Engineering, The University of Electro-Communications, 1-5-1 Chofugaoka, Chofu, Tokyo, 182-8585, Japan

A B S T R A C T

Tin halide perovskites are the front-runner for lead-free perovskite solar cells (PSCs). Currently the highest efficiency is reaching 15% which is the highest among other types of lead-free perovskites. There are several issues with tin halide perovskites that need to be addressed before they can really compete with lead-based PSC. Among the issues are the prone of oxidation of Sn^{2+} into Sn^{4+} in air, fast crystallization leading to morphologically uneven surface and the formation of pinholes, large energy mismatch between commonly used charge transport layers (CTLs), and current-voltage hysteresis due to unbalanced charge carrier transport and ion migration. In this experiment, we incorporated Cs^{+} which is a small A-site cation to reduce the energy mismatch between the perovskite layer and CTLs. Although this was explored previously even in tin halide perovskite solar cells, we showed that Cs cation incorporation alone will not improve the performance, however when used simultaneously with [6,6]-Phenyl-C61 butyric acid butyl ester (PCBM) as the electron transport layer (ETL), we managed to improve the efficiency of the tin PSC to more than 13%. To understand this phenomenon, we used impedance spectroscopy analysis to evaluate the charge transport mechanism. We attribute this enhancement due to better energy level alignment between the perovskite layer and ETL.

1. Introduction

Tin halide perovskite solar cells are slowly catching up with lead halide perovskite solar cells. Recently the highest reported efficiency for tin halide perovskite solar cells has reached 14.81% [1]. There are several challenges that need to be addressed in order for tin halide perovskites to compete with lead halide perovskites [2–4]. Some of the issues are i) oxidation of Sn^{2+}, ii) uncontrolled crystallization, iii) weak Sn–I bond, iv) large energy mismatch between commonly used charge transport layers and v) unbalanced charge transport between holes and electrons.

Through A-site engineering, researchers have managed to address the issues that plagued tin perovskites [5–7]. Although by changing the A-site cation has beneficial effect on the solar cell performance, the efficiency is still unsatisfactory. Example of A-site cation that has been used in tin perovskites is cesium (Cs^{+}). Due to the small ionic size of Cs^{+} (1.67 Å) compared to Formamidinium (FA^{+}) (2.53 Å) and Ethylammonium (EA^{+}) (2.74 Å) ions, the tolerance factor which determine the stability of a perovskite structure can be tuned preferably [8]. Gao et al. performed partial substitution of FA cation with Cs and optimized the Cs ratio to 8 mol % [9]. Compared to the reference device, the device substituted with 8 mol % Cs showed an improvement in the efficiency by up to 63% in addition to improved device lifetime. Tosado et al. introduced guanidinium and cesium cation to achieve pinhole-free cubic phase $FASnI_3$ perovskite layer with suppressed deep and shallow trap states [10].

Even after optimizing A-site cation for tin perovskite solar cells, the average V_{OC} reported is in the range of 0.5–0.6 V. The origin for this low V_{OC} can be attributed to the energy mismatch between Sn-PVK layer and the electron transport layer where C60 fullerene is typically used. Although there are reports using PCBM instead of C60, the V_{OC} is still limited to around 0.6 V. Jiang et al. is the first to report the use of Indene-C60 Bisadduct (ICBA) as an ETL in Sn–PSCs resulting a V_{OC} of more than 0.9 V [3]. However, it is important to note that the authors not only changed the ETL, but also changed the A-site cation such that the conduction band level of the perovskite layer matches that with

* Corresponding author.
** Corresponding author.
*** Corresponding author.
E-mail addresses: akmal-kamarudin@uec.ac.jp (M.A. Kamarudin), shahrir@uec.ac.jp (S.R. Sahamir), hayase@uec.ac.jp (S. Hayase).
[1] Equal contributions.

https://doi.org/10.1016/j.orgel.2022.106712
Received 20 October 2022; Received in revised form 5 December 2022; Accepted 5 December 2022
Available online 7 December 2022

ICBA using 2D precursor Phenethylammonium iodide (PEAI). This has also been supported by other works using similar technique of partial substitution with 2D precursor and ICBA as the ETL [11,12].

In this work, we performed partial substitution of $FAEASnI_3$ with $CsSnI_3$. In addition, we also showed that Cs substitution alone is not sufficient to improve the performance of tin perovskite solar cells. Through synergistic effect of perovskite surface passivation using ethylenediamine and using [6,6]-Phenyl C61 butyric acid methyl ester (PCBM) as the ETL, we have fabricated tin perovskite solar cells with more than 13% efficiency. We attributed this improvement to a more balanced charge transport from perovskite layer into charge transport layers. Simultaneously, the trap density has also been found to be passivated upon partial substitution with Cs.

2. Experimental section

2.1. Materials

Tin (II) iodide (SnI_2, −10 mesh, 99.99% trace metals basis), Tin (II) fluoride (SnF_2, 99%), Formamidinium iodide (FAI, ≥99%, anhydrous), Ethane-1,2-diammonium iodide ($EDAI_2$, ≥98%), Ethylammonium iodide (EAI, 98%), Germanium (II) iodide (GeI_2, ≥99.8% trace metals basis), Cesium iodide (CsI, 99.999% trace metals basis), Fullerene (C_{60}, sublimed, 99.9%), Bathocuproine (BCP, sublimed grade, 99.99% trace metals basis), Phenyl-C61-Butyric-Acid-Methyl Ester (PCBM, >99.9%), Dimethylsulfoxide (DMSO, anhydrous, ≥99.9%), N,N-dimethylformamide (DMF, anhydrous, 99.8%), Chlorobenzene (anhydrous, 99.8%) and Ethylenediamine (ReagentPlus®, ≥99%) were bought from Sigma-Aldrich and used as received. Poly(3,4-ethylenedioxythiophene):polystyrenesulfonate (PEDOT:PSS, CLEVIOS™ P VP AI 4083) was obtained from Heraeus and used as received.

2.2. Device fabrication

Fluorine-doped tin oxide (FTO) glass substrates were washed with deionized water, acetone, and isopropanol (IPA) by ultrasonic bath for 15 min in each solvent, sequentially. Next, the FTO glass substrates were cleaned using oxygen plasma for 5 min. PEDOT:PSS was coated onto the cleaned substrates at 500 rpm for 10 s and 5000 rpm for 40 s followed by heating at 150 °C for 20 min.

Two types of Sn-PVK solutions were prepared using the following recipe:

i) $(FA_{0.9}EA_{0.}1)_{0.98}EDA_{0.01}SnI3$ (1 M SnI_2, 0.882 M FAI, 0.098 M EAI, 0.01 M $EDAI_2$, 0.1 M SnF_2, 0.05 M GeI_2)
ii) $Cs_{0.98}EDA_{0.01}SnI_3$ (1 M SnI_2, 0.98 M CsI, 0.01 M $EDAI_2$, 0.1 M SnF_2, 0.05 M GeI_2)

The two perovskite solutions were mixed according to different ratio. The perovskite solutions were then coated onto the substrates at 5000 rpm for 50 s. Anti-solvent (Chlorobenzene) was dropped at the 15th s from the start of spin-coating process. Next the substrate was baked at 70 °C for 10 min. After cooling the perovskite film to room temperature, 0.5 mM EDA solution prepared in Chlorobenzene was dynamically spin-coated on the perovskite surface, followed by baking at 70 °C for 5 min. For devices with PCBM, 2 mg/ml PCBM solution prepared in Chlorobenzene was coated onto perovskite layer at 5000 rpm for 50 s and baked at 70 °C for 5 min. Next, 30 nm of C_{60}, 7 nm of BCP and 130 nm of Ag were deposited under a high vacuum (10^{-5} Pa) by using physical thermal evaporation.

2.3. Characterizations

UV–Vis measurements were performed using a JASCO V-670 Spectrophotometer with the samples prepared on optically smooth glass substrates. Valence band level was determined by photoelectron yield spectroscopy (PYS) using Bunkoukeiki KV 205-HK ionization energy system using photon energy ranging from 4.0 eV to 6.5 eV with the samples prepared on PEDOT:PSS-coated FTO substrates. X-ray diffraction (XRD) pattern was obtained by using XRD system RINT-ULTIMA III, RIGAKU with Cu Kα radiation (λ = 1.54 Å) with the samples prepared on PEDOT:PSS-coated FTO substrates. Photoluminescence (PL) and time-resolved PL decay were evaluated by compact photoluminescence lifetime spectrometer (Quantaurus C-11367, HAMAMATSU Photonics, Japan) with the samples prepared on optically smooth glass substrates. X-ray photoelectron spectroscopy (XPS) was conducted with JPS-9200, JEOL Ltd with the samples prepared on PEDOT:PSS-coated FTO substrates. Carrier density, mobility, and conductivity were measured by Hall-effect measurement (Ecopia Co., HMS-3000). Samples for Hall effect measurement were prepared on platinum (Pt)-sputtered glass having a cross-slit (width: 2 μm). The current density-voltage (J-V) characteristics of the perovskite solar cells were measured using an integrated solar simulator (JIS C 8942 Class MA). Solar cell performance was characterized under illumination by a standard amorphous Si photodetector (BS 520 S/N 007, Bunko Keiki, Japan) an air mass 1.5 global (AM 1.5G) solar simulator with an irradiation intensity of 100 mW cm^{-2} 0.1 cm^2 size apertures made of thin metal were attached to each cell before measurement. Further, the solar spectrum was controlled to 1 sun light illumintaion using a spectroradiometer (LS-100, Eiko, Seiki, Japan). The external quantum efficiencies (EQEs) were obtained using a module equipped with monochromated light from a Xe arc lamp in the same solar simulator with direct current mode without any biasing using monochromatic light from 1000 nm to 300 nm (Newport 74010) under a constant photon flux of 1×10^{16} photon cm^{-2} at each wavelength. The current versus voltage characteristics were obtained in forward and reverse scan (0.1 V s^{-1}) under the simulated solar spectrum.

3. Result and discussion

In Fig. 1a, we show the XRD data for $((FA_{0.9}EA_{0.1})_{1-x}Cs_x)_{0.98}SnI_3$ where x = 0.02, 0.04, 0.06, and 0.08. For simplification, we use the following name for our samples: Cs 0, Cs 2, Cs 4, Cs 6 and Cs 8. The overall shape of XRD data remains the same after partial substitution with Cs ion, which suggest that the perovskite retain its cubic structure. However, upon closer inspection of the peak around 13.80°(Fig. 1b), we could see that the peak belongs to (110) facet is shifting towards larger angle upon Cs cation substitution. This has been explained previously by other works where they describe this observation due to larger Cs cation incorporated within the perovskite lattice resulting in lattice contraction [13]. Evaluation of the lattice spacing indeed showed the perovskite experience lattice compression where lattice spacing for Cs 0 sample is 6.7 Å while for Cs 8 is 6.6 Å. Another interesting thing to note is the increased in the XRD peak intensity which qualitatively means that the perovskite quality has improved upon Cs substitution.

Fig. 1c shows the UV–Vis absorption of perovskite films with various Cs content. Increasing Cs content leads to a red-shift of the absorption spectra. Using Tauc plot, we determined the bandgap, E_g for each sample. We found that E_g decreases with higher Cs content. This can be explained by lattice contraction upon Cs substitution resulting in increased metal-halide orbital overlap which has been reported previously by Prasanna et al. [13]. Using photoelectron yield spectroscopy (PYS) measurements, we determined the valence band energy of the perovskite films. Upon Cs substitution, the valence band level shifted to shallower energy levels. With E_g values obtained from UV–Vis measurements and valence band levels from PYS measurements (Fig. S1), we constructed the energy level diagram (Fig. 1d) consisting of various perovskite solar cell components. The valence band energy is shifting closer towards PEDOT:PSS, thus the energy barrier for hole injection from perovskite layer into PEDOT:PSS is getting smaller and we could expect a more efficient hole injection. However, as the energy levels becoming shallower, energy gap mismatch between the conduction

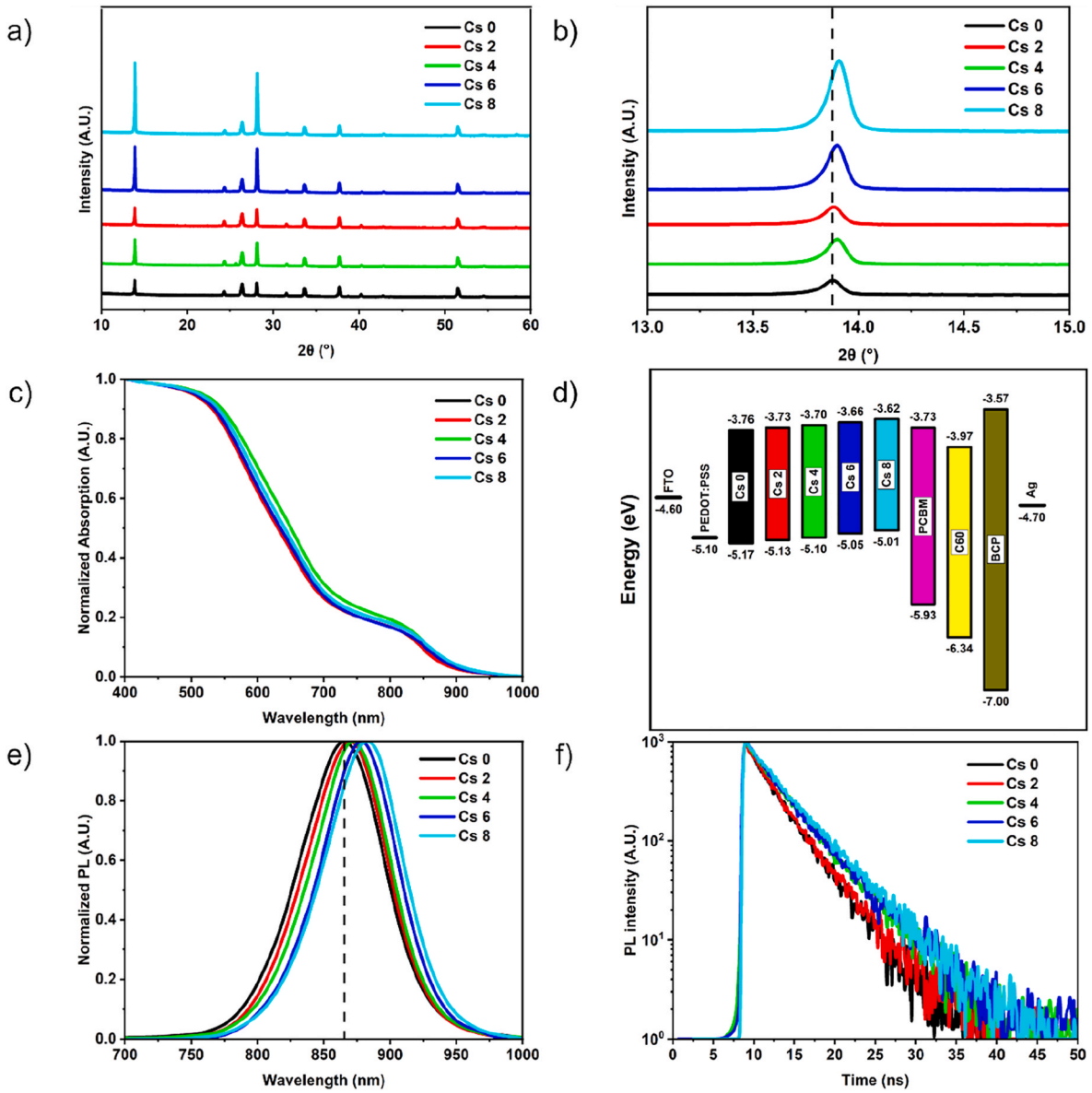

Fig. 1. a) Broad XRD peak and b) narrow XRD peak of Cesium-substituted $FAEASnI_3$ perovskite layer. c) UV–Vis absorption of perovskite films with different ratio of cesium. d) energy diagram consisting various components in Sn-based perovskite solar cells. e) Steady-state PL spectra and f) the corresponding time-resolved PL of various Sn-PVK films.

band of perovskite layer and C_{60} fullerene is becoming bigger. As the energy barrier is bigger in this case, instead of electrons being injected into electron transport layer, the accumulation of electrons in the perovskite layer will lead to higher chance of charge carrier recombination. The issue of energy mismatch at perovskite/C_{60} interface has been discussed previously by Hu et al. [14]. To overcome this issue, we proposed electron transport bilayer structure using PCBM and C_{60} fullerene to minimize the energy mismatch between perovskite layer and ETL. The conduction band (C.B.) of PCBM is −3.73 eV which is shallower than that of C_{60} (- 3.97 eV). Thus, we anticipate the V_{OC} to be enhanced significantly using PCBM/C_{60} bilayer. Work by Lee et al. indeed supported our hypothesis that the energy mismatch significantly affect the V_{OC} in tin-based perovskite solar cells and by changing the n-type material, higher V_{OC} can be obtained [11].

Fig. 1e shows the steady state and time-resolved photoluminescence results for Sn-PVKs with various Cs concentration. The PL emission peaks supports the UV–Vis results where increasing Cs content in the perovskite gradually increased the peaks to higher wavelength. From the TRPL plot (Fig. 1f), using a biexponential decay fit, we estimated the charge carrier lifetime to be 3.50 ns (Cs 0), 3.67 ns (Cs 2), 4.35 ns (Cs 4), 4.37 ns (Cs 6) and 4.56 ns (Cs 8) as summarized in Table 1. The fast decay can be attributed to non-radiative charge carrier trapping while the slower decay is caused by radiative recombination [15,16]. Thus, it can be safely assumed that enhancement of photovoltaic performance upon Cs introduction can be partly attributed to suppression of defect/trap sites within the perovskite layer.

The effect of Cs substitution on perovskite solar cell performance is

Table 1
Summary of PL peak and carrier lifetime of various perovskite layers.

Sample	PL peak (nm)	τ_{ave} (ns)	τ_1 (ns)	τ_2 (ns)
Cs 0	865	3.50	0.96	3.63
Cs 2	869	3.67	2.05	3.99
Cs 4	871	4.35	1.96	4.58
Cs 6	877	4.37	2.16	4.79
Cs 8	882	4.56	1.34	4.67

investigated using the following device structure: FTO/PEDOT:PSS/Sn-PVK/C_{60}/BCP/Ag. Fig. S2a shows the J-V plot for the champion device for each condition. The best reference device showed efficiency of 10.75% and upon introducing 2 mol % Cs the efficiency improved to 11.61%, 11.74% for 4 mol% Cs, 10.97% for 6 mol % Cs and 10.24% for 8 mol % as summarized in Table 2. The optimum Cs concentration is found to be 4 mol % in which all device parameters including open-circuit voltage (V_{OC}), short-circuit current (J_{SC}) and fill factor (FF) showed significant improvement compared to the reference device. We observed that higher Cs content gives higher V_{OC} which can be explained from better energy level alignment between perovskite layer and charge transport layers as shown from energy level diagram. To confirm the reliability of this experiment, we fabricated more than 15 devices for each condition and summarized the result in Tables S1–S2. We showed the device parameter distribution in Figs. S2b–2e where the plot showed similar trend to that observed in the champion *J-V*. The increase in J_{SC} can be explained from the blue-shift of UV–Vis absorption suggesting increased light absorption window which in turn can be turned into photogenenerated electrons. However, there is still a large V_{OC} (~0.84 V) loss observed in these devices which we attributed to the energy mismatch at the Sn-PVK/n-type material interface. Fig. S3a shows the *J-V* plot of the champion device using PCBM/C_{60} bilayer ETL. The reference device showed the highest efficiency of 10.75% while the optimized device of Cs 4 has an efficiency of 11.74%. As we have expected, the V_{OC} increased significantly reaching as high as 0.74 V (V_{OC} loss 0.66 V). As a result, the average efficiency improved to nearly 11%. However, when PCBM is employed as the ETL, J_{SC} slightly reduced (~22 mA cm^{-2}) compared to only when C_{60} is used (~23 mA cm^{-2}). This can be explained due to the lower electron mobility in the case of PCBM [17]. Furthermore, according to Namkoong et al., in addition to facilitating charge transfer in PSCs, PCBM/C_{60} bilayer ETL also helped to suppress defect sites at the perovskite interface which can also explain the V_{OC} increase [18]. We have summarized the device parameter distribution in Figs. S3b–3e. To better understand the effect of Cs substitution and the use of PCBM/C_{60} bilayer, we have compiled the data in Fig. 2.

After storage under dark condition for 1 week, we measured again the performance of the champion Cs 4 device. Fig. 3a shows the *J-V* curve. The performance increased from 11% to 13.32% as a result of improved V_{OC} and FF as summarized in Table 3. This enhanced efficiency after storage is unique to Sn-PVK solar cells and has been reported previously by other works [19,20]. Relaxation of lattice strain upon storage has been cited as the reason for this enhancement. In addition, we also performed maximum power point tracking (MPPT) measurements as shown in Fig. S4. There is no degradation in device performance even after 20 min showing the superior stability of the cesium-substituted device. We also performed external quantum efficiency (EQE) measurements (Fig. 3b) to check the reliability of the measured J_{SC}. The calculated J_{SC} from EQE measurements agrees well with the measured J_{SC} where the error is within 2%.

We performed dark current analysis for Cs 0 and Cs 4 devices to further understand the origin of this improvement. Following previous works, dark current analysis will provide information such as the ideality factor, *n* and dark saturated current, J_0 using the following equations

$$-\frac{dV}{dJ} = \frac{nk_BT}{q}(J_{SC} - J)^{-1} + R_s$$

$$ln(J_{SC} - J) = \frac{q}{nk_BT}(V + R_sJ) + ln\, J_0$$

where n is the ideality factor where an ideal diode will have an ideality factor of 0 [21,22]. As a comparison, Cs 0 device showed higher ideality factor of 1.95 compared to 1.75 for Cs 4 device. Higher ideality factor has been attributed to non-radiative recombination process originated from trap-mediated recombination. This indirectly shows that Cs 4 has lower trap density compared to Cs 0. In addition, the calculated dark saturated current density for Cs 4 is 2 order magnitude lower than Cs 0. J_0 is also an important parameter that is related to the defect density [23]. For tin perovskites, it is commonly agreed that it is intrinsically p-type due to easy oxidation of Sn^{2+} into Sn^{4+} which will increase the background hole carrier concentration [24]. It can be safely inferred that the hole carrier density is lower in the case of Cs 4 device judging from the lower J_0.

To further validate the charge transfer process within the perovskite solar cells, we carried out electrochemical impedance spectroscopy (EIS) measurements which is a well-known method to understand the charge transfer dynamics at various time scales within a solar cell [4]. Here, we performed the measurements under 1 sun light illumination at various applied voltage for Cs 0 and Cs 4 devices. Comparing the geometric capacitance values between Cs 0 (~10^{-5} F cm^{-2}) and Cs 4 (~10^{-6} F cm^{-2}), incorporation of Cs reduced the geometric capacitance by one order of magnitude. This means that the ionic accumulation within the perovskite has been significantly reduced [26,27].

We investigated the effect of cesium substitution on Sn metal using XPS measurements. Fig. 4e and f shows the Sn 3d5/2 peak comparing Cs 0 and Cs 4 samples. Deconvolution of the peak using Voigt fitting, we estimated the ratio of Sn^{2+} and Sn^{4+} species and summarized the results in Table 4. For Cs 0, Sn^{2+}:Sn^{4+} ratio is 78.3:21.7, while for Cs 4, the ratio is 82.3:17.7. Clearly, the incorporation of Cs suppressed the oxidation of Sn (less p-doping due to Sn^{4+}). This helps to explain the decrease of p-type carrier from the Hall effect measurements. In addition to better energy alignment between the perovskite layer and CTL, the reduction of p-type charge carrier originating from Sn^{4+} helped to decrease the charge carrier recombination and hence improved the V_{OC}. The presence of Cs in the perovskite layer has also been confirmed from the XPS measurements. Fig. S5 shows the Cs $3d_{3/2}$ and $3d_{5/2}$ peaks for Cs 4 sample, while for Cs 0 sample no peak is observed.

Using Hall effect measurement system, we evaluated the Hall mobility and charge carrier concentration of Cs 0 and Cs 4 perovskites (Table 5). Both samples showed p-type behavior which is as expected since Sn-PVKs are known to be p-doped [28,29]. The charge carrier mobilities measured for Cs 0 and Cs 4 are 1.51 $cm^2\ V^{-1}\ s^{-1}$ and 6.12 $cm^2\ V^{-1}\ s^{-1}$, respectively. Additionally, the carrier concentration decreased by one order of magnitude from 8.24×10^{16} cm^{-3} for Cs 0 to 8.50×10^{15} cm^{-3} for Cs 4. Lower charge carrier concentration has been explained as one of the reasons for increasing the carrier mobility as reported previously by Motta et al. [30]. Another reason for this enhanced charge carrier mobility is due to the suppression of trap states within the perovskite layer [31]. This also indirectly supports our result which showed higher V_{OC} upon partial substitution with Cs.

Table 2
Summary of photovoltaic parameters of Cs 0 and Cs 4 using PCBM/C_{60} bilayer and C_{60} single ETL.

Sample	Efficiency (%)	FF	V_{OC} (V)	J_{SC} (mA cm^{-2})
Cs 0/C60	8.44	0.61	0.61	22.64
Cs 4/C60	8.17	0.62	0.56	23.22
Cs 0-PCBM/C60	10.50	0.72	0.68	21.24
Cs 4-PCBM/C60	11.74	0.74	0.71	22.18

4. Conclusion

In conclusion, we have demonstrated that a small amount of Cs incorporated into $FASnI_3$ could suppress the oxidation of Sn^{2+} and this was the result of lowering the energy levels of Sn-PVK layers. However, this alone will not help to increase the efficiency. We also showed that by introducing ETL bilayer consisting of PCBM and C60, higher V_{OC} can be obtained. We discussed this from smaller energy mismatch between the perovskite layer and ETL. Additionally, our results revealed that lower

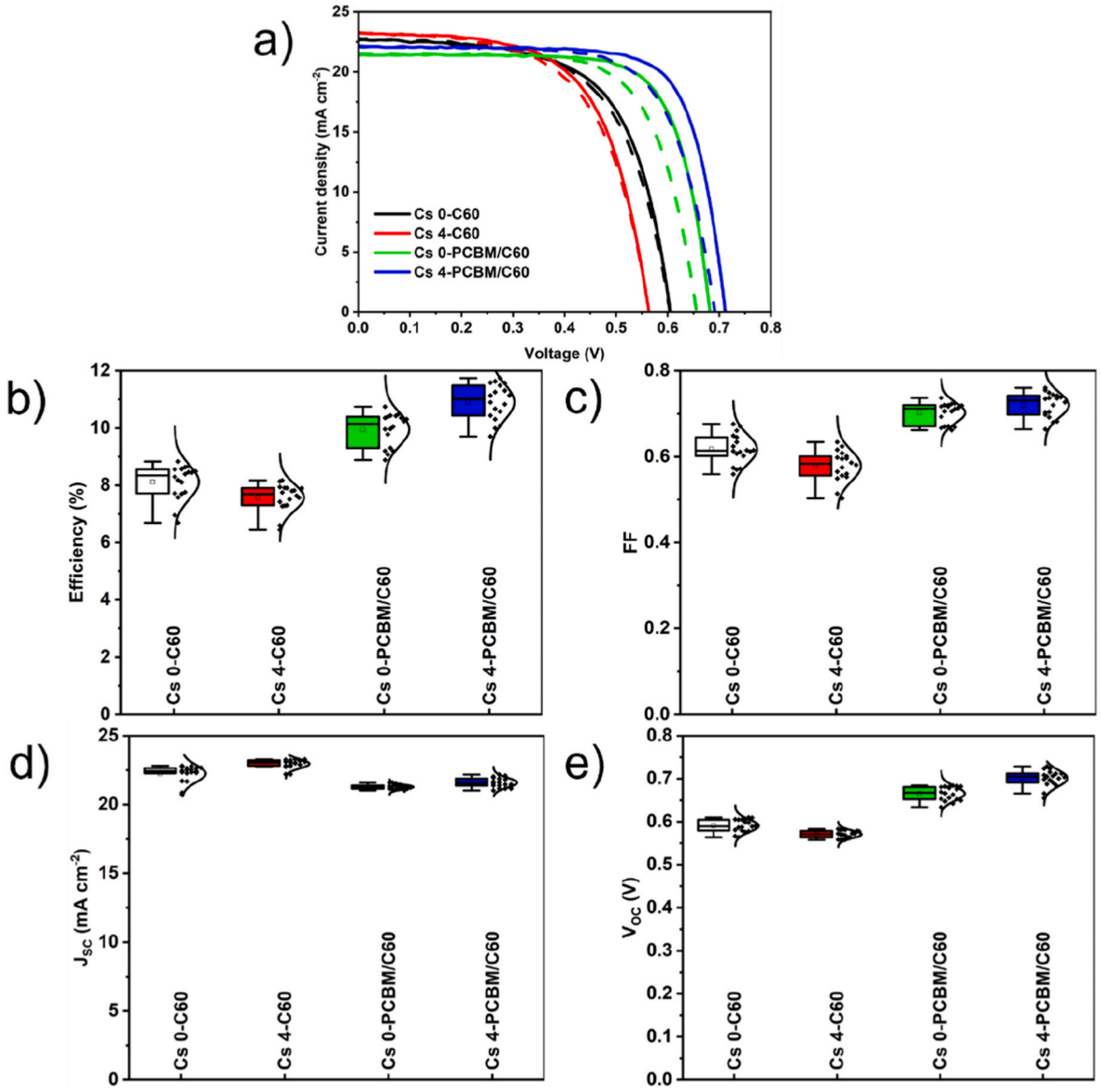

Fig. 2. a) Champion *J-V* of Cs 0 and Cs 4 comparing C60 and PCBM/C60 electron transport layers. Device parameter distribution of b) efficiency, c) FF, d) J_{SC} and e) V_{OC}.

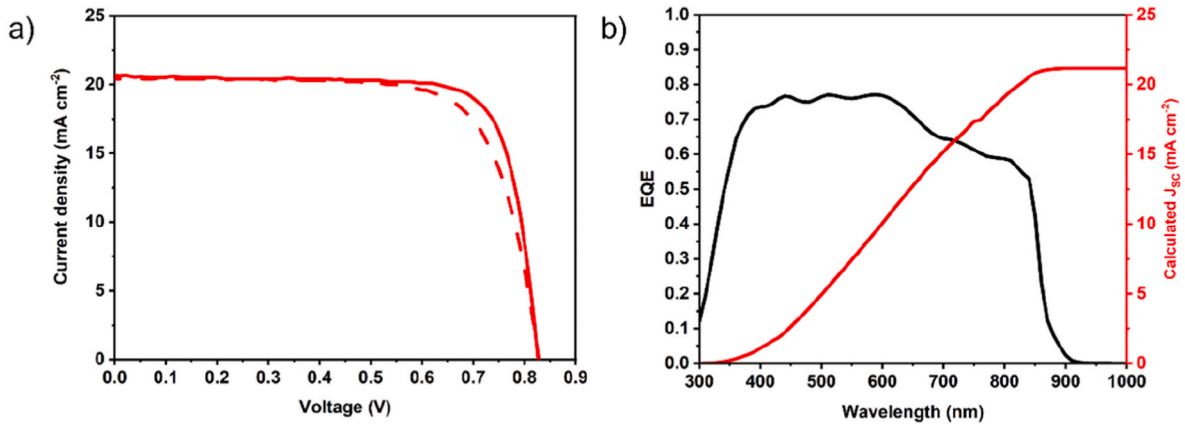

Fig. 3. a) *J-V* curve of champion Cs 4 device after storage under dark condition for 1 week and b) the corresponding EQE spectra. Solid and dotted line refer to the forward scan and reverse scan, respectively.

Table 3
Summary of photovoltaic properties of champion Cs 4 device.

Sample	Efficiency (%)	FF	V_{OC} (V)	J_{SC} (mA cm^{-2})
Forward	13.32	0.779	0.827	20.69
Reverse	12.39	0.732	0.828	20.43

hole carrier concentration has been achieved with Cs substitution and thus reducing charge carrier recombination. As a result, we have fabricated Sn-PVK solar cell showing 13.39% efficiency with V_{OC} of 0.828 V. Our work showed that substituting the A-site cation alone might show a negative trend but by simultaneously changing the ETL will have a beneficial effect on the device performance.

Declaration of competing interest

The authors declare that they have no known competing financial

Table 4
Summary of Sn species for Cs 0 and Cs 4 samples.

Sample	Sn^{2+} (%)	Sn^{4+} (%)
Cs 0	78.3	21.7
Cs 4	82.3	17.7

Table 5
Summary of carrier density and mobility obtained using Hall effect measurements.

Sample	Carrier density (cm^{-3})	μ (cm^2 V^{-1} s^{-1})
Cs 0	8.24×10^{16}	1.51
Cs 4	8.50×10^{15}	6.12

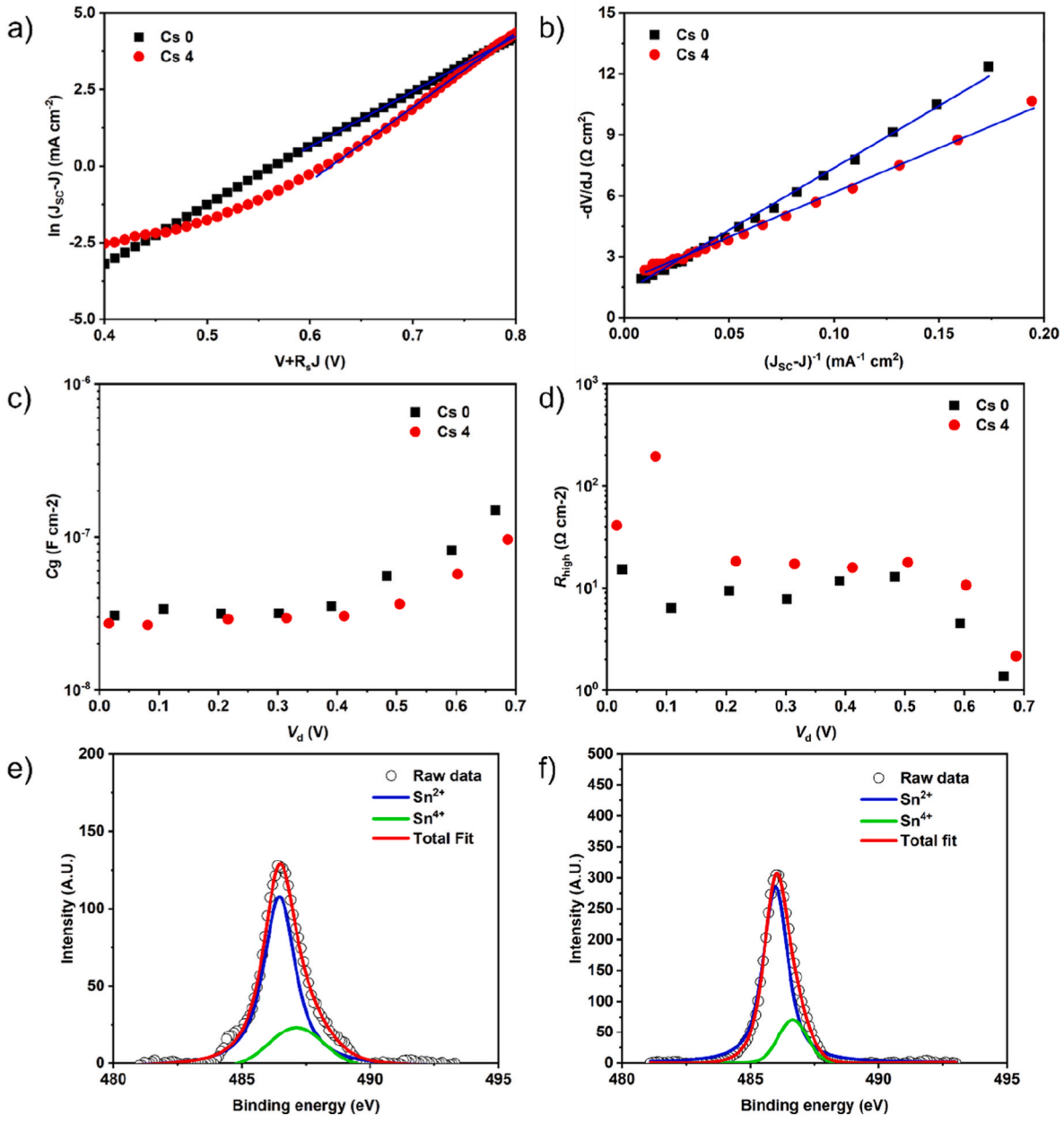

Fig. 4. a) Plots of ln (J_{SC} - J) as a function of $V + R_sJ$ and b) -(dV/dJ) as a function of (J_{SC} - J)$^{-1}$. c) Geometric capacitance and d) resistance at high frequency as a function of applied voltage. Measurements performed under 1 sun light illumination. XPS plot of Sn 3d5/2 peak of e) Cs 0 and f) Cs 4 perovskite layers.

interests or personal relationships that could have appeared to influence the work reported in this paper.

Data availability

The authors do not have permission to share data.

Appendix A. Supplementary data

Supplementary data to this article can be found online at https://doi.org/10.1016/j.orgel.2022.106712.

References

[1] B.-B. Yu, Z. Chen, Y. Zhu, Y. Wang, B. Han, G. Chen, X. Zhang, Z. Du, Z. He, Heterogeneous 2D/3D tin-halides perovskite solar cells with certified conversion efficiency breaking 14, Adv. Mater. 33 (2021), 2102055, https://doi.org/10.1002/adma.202102055.

[2] L. Lanzetta, T. Webb, N. Zibouche, X. Liang, D. Ding, G. Min, R.J.E. Westbrook, B. Gaggio, T.J. Macdonald, M.S. Islam, S.A. Haque, Degradation mechanism of hybrid tin-based perovskite solar cells and the critical role of tin (IV) iodide, Nat. Commun. 12 (2021) 2853, https://doi.org/10.1038/s41467-021-22864-z.

[3] X. Jiang, F. Wang, Q. Wei, H. Li, Y. Shang, W. Zhou, C. Wang, P. Cheng, Q. Chen, L. Chen, Z. Ning, Ultra-high open-circuit voltage of tin perovskite solar cells via an electron transporting layer design, Nat. Commun. 11 (2020) 1245, https://doi.org/10.1038/s41467-020-15078-2.

[4] M. Aldamasy, Z. Iqbal, G. Li, J. Pascual, F. Alharthi, A. Abate, M. Li, Challenges in tin perovskite solar cells, Phys. Chem. Chem. Phys. 23 (2021) 23413–23427, https://doi.org/10.1039/D1CP02596A.

[5] W. Gao, C. Chen, C. Ran, H. Zheng, H. Dong, Y. Xia, Y. Chen, W. Huang, A-site cation engineering of metal halide perovskites: version 3.0 of efficient tin-based lead-free perovskite solar cells, Adv. Funct. Mater. 30 (2020), 2000794, https://doi.org/10.1002/adfm.202000794.

[6] J. Sanchez-Diaz, R.S. Sánchez, S. Masi, M. Krečmarová, A.O. Alvarez, E.M. Barea, J. Rodriguez-Romero, V.S. Chirvony, J.F. Sánchez-Royo, J.P. Martinez-Pastor, I. Mora-Seró, Tin perovskite solar cells with >1,300 h of operational stability in N2 through a synergistic chemical engineering approach, Joule 6 (2022) 861–883, https://doi.org/10.1016/j.joule.2022.02.014.

[7] C.-H. Kuan, J.-M. Chih, Y.-C. Chen, B.-H. Liu, C.-H. Wang, C.-H. Hou, J.-J. Shyue, E. W.-G. Diau, Additive engineering with triple cations and bifunctional sulfamic acid for tin perovskite solar cells attaining a PCE value of 12.5% without hysteresis, ACS Energy Lett. (2022) 4436–4442, https://doi.org/10.1021/acsenergylett.2c02148.

[8] G. Han, H.D. Hadi, A. Bruno, S.A. Kulkarni, T.M. Koh, L.H. Wong, C. Soci, N. Mathews, S. Zhang, S.G. Mhaisalkar, Additive selection strategy for high performance perovskite photovoltaics, J. Phys. Chem. C 122 (2018) 13884–13893, https://doi.org/10.1021/acs.jpcc.8b00980.

[9] W. Gao, C. Ran, J. Li, H. Dong, B. Jiao, L. Zhang, X. Lan, X. Hou, Z. Wu, Robust stability of efficient lead-free formamidinium tin iodide perovskite solar cells realized by structural regulation, J. Phys. Chem. Lett. 9 (2018) 6999–7006, https://doi.org/10.1021/acs.jpclett.8b03194.

[10] G.A. Tosado, E. Zheng, Q. Yu, Tuning cesium–guanidinium in formamidinium tin triiodide perovskites with an ethylenediammonium additive for efficient and stable lead-free perovskite solar cells, Mater Adv 1 (2020) 3507–3517, https://doi.org/10.1039/D0MA00520G.

[11] M. Lee, D. Kim, Y. Kyu Lee, H. Koo, K. Tae Lee, I. Chung, Indene-C60 Bisadduct electron-transporting material with the high LUMO level enhances open-circuit voltage and efficiency of tin-based perovskite solar cells, ACS Appl. Energy Mater. 3 (2020) 5581–5588, https://doi.org/10.1021/acsaem.0c00535.

[12] X. Jiang, H. Li, Q. Zhou, Q. Wei, M. Wei, L. Jiang, Z. Wang, Z. Peng, F. Wang, Z. Zang, K. Xu, Y. Hou, S. Teale, W. Zhou, R. Si, X. Gao, E.H. Sargent, Z. Ning, One-step synthesis of SnI2·(DMSO)x adducts for high-performance tin perovskite solar cells, J. Am. Chem. Soc. 143 (2021) 10970–10976, https://doi.org/10.1021/jacs.1c03032.

[13] R. Prasanna, A. Gold-Parker, T. Leijtens, B. Conings, A. Babayigit, H.-G. Boyen, M. F. Toney, M.D. McGehee, Band gap tuning via lattice contraction and octahedral tilting in perovskite materials for photovoltaics, J. Am. Chem. Soc. 139 (2017) 11117–11124, https://doi.org/10.1021/jacs.7b04981.

[14] X. Hu, C. Liu, Z. Zhang, X.-F. Jiang, J. Garcia, C. Sheehan, L. Shui, S. Priya, G. Zhou, S. Zhang, K. Wang, 22% efficiency inverted perovskite photovoltaic cell using cation-doped brookite TiO2 top buffer, Adv. Sci. 7 (2020), 2001285, https://doi.org/10.1002/advs.202001285.

[15] H.-C. Kwon, W. Yang, D. Lee, J. Ahn, E. Lee, S. Ma, K. Kim, S.-C. Yun, J. Moon, Investigating recombination and charge carrier dynamics in a one-dimensional nanopillared perovskite absorber, ACS Nano 12 (2018) 4233–4245, https://doi.org/10.1021/acsnano.7b07559.

[16] Y. Zhang, S.-G. Kim, D. Lee, H. Shin, N.-G. Park, Bifacial stamping for high efficiency perovskite solar cells, Energy Environ. Sci. 12 (2019) 308–321, https://doi.org/10.1039/C8EE02730G.

[17] C. Cui, Y. Li, Y. Li, Fullerene derivatives for the applications as acceptor and cathode buffer layer materials for organic and perovskite solar cells, Adv. Energy Mater. 7 (2017), 1601251, https://doi.org/10.1002/aenm.201601251.

[18] G. Namkoong, A.A. Mamun, T.T. Ava, Impact of PCBM/C60 electron transfer layer on charge transports on ordered and disordered perovskite phases and hysteresis-free perovskite solar cells, Org. Electron. 56 (2018) 163–169, https://doi.org/10.1016/j.orgel.2018.02.010.

[19] E. Jokar, P.-Y. Cheng, C.-Y. Lin, S. Narra, S. Shahbazi, E. Wei-Guang Diau, Enhanced performance and stability of 3D/2D tin perovskite solar cells fabricated with a sequential solution deposition, ACS Energy Lett. 6 (2021) 485–492, https://doi.org/10.1021/acsenergylett.0c02305.

[20] E. Jokar, C.H. Chien, A. Fathi, M. Rameez, Y.H. Chang, E.W.G. Diau, Slow surface passivation and crystal relaxation with additives to improve device performance and durability for tin-based perovskite solar cells, Energy Environ. Sci. 11 (2018) 2353–2362, https://doi.org/10.1039/c8ee00956b.

[21] W. Tress, M. Yavari, K. Domanski, P. Yadav, B. Niesen, J.P. Correa Baena, A. Hagfeldt, M. Graetzel, Interpretation and evolution of open-circuit voltage, recombination, ideality factor and subgap defect states during reversible light-soaking and irreversible degradation of perovskite solar cells, Energy Environ. Sci. 11 (2018) 151–165, https://doi.org/10.1039/C7EE02415K.

[22] Y. Li, B. Ding, Q.-Q. Chu, G.-J. Yang, M. Wang, C.-X. Li, C.-J. Li, Ultra-high open-circuit voltage of perovskite solar cells induced by nucleation thermodynamics on rough substrates, Sci. Rep. 7 (2017), 46141, https://doi.org/10.1038/srep46141.

[23] C. Li, Z. Song, D. Zhao, C. Xiao, B. Subedi, N. Shrestha, M.M. Junda, C. Wang, C. S. Jiang, M. Al-Jassim, R.J. Ellingson, N.J. Podraza, K. Zhu, Y. Yan, Reducing saturation-current density to realize high-efficiency low-bandgap mixed tin–lead halide perovskite solar cells, Adv. Energy Mater. 9 (2019), https://doi.org/10.1002/aenm.201803135.

[24] S.J. Lee, S.S. Shin, J. Im, T.K. Ahn, J.H. Noh, N.J. Jeon, S. il Seok, J. Seo, Reducing carrier density in formamidinium tin perovskites and its beneficial effects on stability and efficiency of perovskite solar cells, ACS Energy Lett. 3 (2018) 46–53, https://doi.org/10.1021/acsenergylett.7b00976.

[26] B. Chen, M. Yang, X. Zheng, C. Wu, W. Li, Y. Yan, J. Bisquert, G. Garcia-Belmonte, K. Zhu, S. Priya, Impact of capacitive effect and ion migration on the hysteretic behavior of perovskite solar cells, J. Phys. Chem. Lett. 6 (2015) 4693–4700, https://doi.org/10.1021/acs.jpclett.5b02229.

[27] D. Prochowicz, M.M. Tavakoli, A.Q. Alanazi, S. Trivedi, H. Tavakoli Dastjerdi, S. M. Zakeeruddin, M. Grätzel, P. Yadav, Charge accumulation, recombination, and their associated time scale in efficient (GUA)x(MA)1–xPbI3-Based perovskite solar cells, ACS Omega 4 (2019) 16840–16846, https://doi.org/10.1021/acsomega.9b01701.

[28] S. Jana, E. Carlos, S. Panigrahi, R. Martins, E. Fortunato, Toward stable solution-processed high-mobility p-type thin film transistors based on halide perovskites, ACS Nano 14 (2020) 14790–14797, https://doi.org/10.1021/acsnano.0c02862.

[29] I. You, Y.-Y. Noh, Toward high-performance p-type, tin-based perovskite thin film transistors, Appl. Phys. Lett. 118 (2021), 250501, https://doi.org/10.1063/5.0051382.

[30] C. Motta, F. El-Mellouhi, S. Sanvito, Charge carrier mobility in hybrid halide perovskites, Sci. Rep. 5 (2015), 12746, https://doi.org/10.1038/srep12746.

[31] T. Leijtens, G.E. Eperon, A.J. Barker, G. Grancini, W. Zhang, J.M. Ball, A.R. S. Kandada, H.J. Snaith, A. Petrozza, Carrier trapping and recombination: the role of defect physics in enhancing the open circuit voltage of metal halide perovskite solar cells, Energy Environ. Sci. 9 (2016) 3472–3481, https://doi.org/10.1039/C6EE01729K.